1. DESCRIPTION OF THE PHYSICAL PROBLEM

The studies of collisions involving weakly bound nuclei at energies around and below the Coulomb barrier arose a considerable interest in the last decade. As already introduced, the very low break-up threshold, which characterizes these nuclei, implies that direct processes are more relevant. Moreover, their diffused surface affects the shape of the projectile-target potential reducing the Coulomb barrier. Such kind of collisions have been studied in order to understand the effects on different reaction channels due to the coupling to the continuum that, in the case of weakly bound nuclei, is very close to the ground state.

It is indeed well known that the fusion process does not depend only on the one-dimensional potential between the two colliding nuclei but is influenced by the internal degrees of freedom of the participants and therefore by the coupling to other reaction channels. Moreover it has been observed that the coupling to the continuum also affects the elastic scattering.

In this chapter, after a general discussion of the fusion process above and below the Coulomb barrier, the expected effects on fusion and elastic scattering involving weakly bound nuclei will be discussed.

1.1 The fusion process above the Coulomb barrier

The complete fusion of two colliding nuclear systems happens when the consequence of the collision is the formation of a compound nucleus (CN), which has a number of nucleons equal to the sum of the nucleons of the participants. The compound nucleus (CN) is an excited spinning system in statistical equilibrium that "lives" for $\sim 10^{-20} \div 10^{-18}$ seconds. This time is long enough to allow the uniform distribution of the compound nucleus excitation energy to all its nucleons, loosing memory of its formation, except for the effects due to the angular momentum conservation. After this period of time the compound nucleus releases its excitation energy and its spin by fission or emitting particles and gamma rays [15]. This process, as schematically shown in Fig 1.1, leads to an evaporation residue (ER) or to fission fragments.

The compound nucleus formed by the collision of sufficiently light systems has a negligible probability to decay through fission so the fusion cross-section for light systems corresponds to the ER production cross-section. The effective potential between two colliding nuclei is the sum of the nuclear potential, the Coulomb electrostatic potential and the centrifugal potential. As a function of the distance between the two participants, the

effective potential shows a relative maximum, which for l=0 is the so-called Coulomb barrier. As can be seen in fig 1.2, the fusion cross-section trend, emerging from a systematic study of a large number of reactions, shows three different behaviors as a function of the inverse center-of-mass energy.

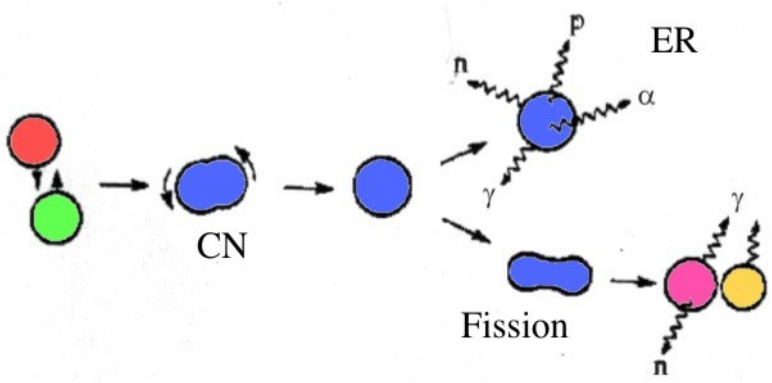

Fig. 1.1 *Schematic representation of fusion. After its formation the compound nucleus releases its excitation energy and its spin emitting particles and gamma rays and leaving an ER or a fission fragment.*

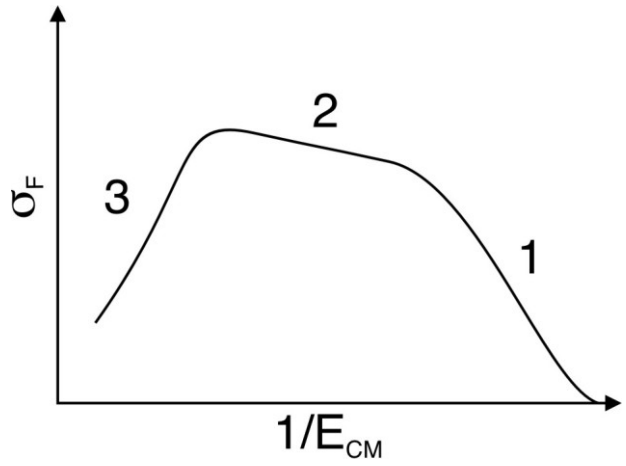

Fig. 1.2 *Schematic representation of the three regions of the fusion cross-section.*

1.1.1 Region 1

The first energy region lies slightly above the Coulomb barrier. In this region only the collisions corresponding to partial waves such that the center-of-mass energy is greater than the barrier generated by the effective potential will lead to the fusion. The fusion cross-section rises up with the center-of-mass energy and is approximately equal to the total reaction cross-section until the non-fusion processes induced by the strong force start to compete with the fusion one. The fusion cross-section in this first region can be easily

explained in a semi-classical model that describes the nuclei as rigid spheres interacting by a potential that involves just the radial distance between the centers of mass of the two objects. This potential contains a Coulomb repulsive term V_C, a centrifugal term V_r and an attracting nuclear term V_N:

$$V_l(r)=V_C(r)+V_r(r,l)+V_N(r) \tag{1.1}$$

In fig.1.3 is shown the potential trend as a function of the distance between the colliding nuclei.

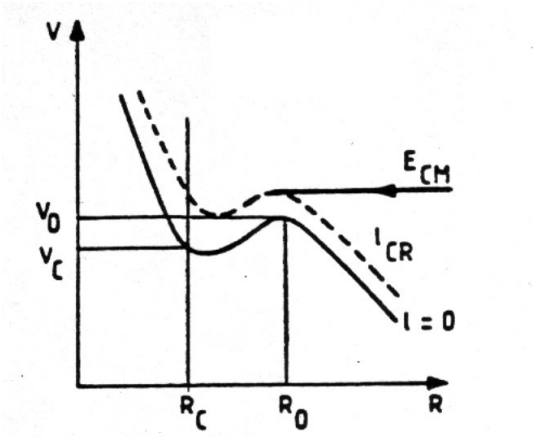

Fig 1.3 *Effective potential between two colliding nuclei as the sum of the electrostatic repulsive term, the centrifugal term and the nuclear term. All the partial waves from l=0 to l=l_{CR} contribute to the fusion process.*

Since to each partial wave is associated a relative angular momentum l, the already mentioned condition can be described introducing a maximum relative angular momentum l_{CR} such that the partial waves with $l<l_{CR}$ contribute to the fusion. Hence l_{CR} satisfies the condition:

$$V_{lcr}[R_{lcr}]=E \tag{1.2}$$

Where E is the center-of-mass energy and V_{lcr} (R_{lcr}) is the effective potential value calculated for $l=l_{cr}$ in its maximum that is $R=R_{lcr}$. The formula (1.2) can be written

$$V_{NC}\left[R_{l_{cr}}\right]+\frac{l_{cr}(l_{cr}+1)\hbar^2}{2\mu R_{l_{cr}}^2}=E \tag{1.3}$$

where μ is the reduced mass of the system and V_{NC} is the sum of the nuclear potential and the Coulomb one. Equation (1.3) allows to obtain an explicit formula for the fusion cross-section with the approximation $(l_{cr}+1)^2 \sim l_{cr}(l_{cr}+1)$.

$$\sigma_{fus}=\frac{\pi}{k^2}(l_{cr}+1)^2=\frac{\pi}{k^2}\frac{2\mu R_{l_{cr}}^2}{\hbar^2}\left[E-V_{NC}\right] \tag{1.4}$$

Since the position R of the barrier depends slightly on l, one may set $R_0=R(l_{cr})$ and, since is

$$E=\frac{\hbar^2 k^2}{2\mu} \tag{1.5}$$

one obtains:

$$\sigma_{fus}=\pi R_0^2\left[1-\frac{V_{NC}(R_0)}{E}\right] \tag{1.6}$$

where, as already mentioned, R_0 is the barrier position for l=0, $V_{NC}(R_0)$ is the sum of the nuclear potential and the Coulomb one calculated in R_0 and E is the center-of-mass energy. This formula shows that σ_f is a linear function of the inverse center-of-mass energy, as observed from the experimental systematic.

1.1.2 Region 2 and 3

The competition between the fusion and the non-fusion processes induced by the strong force becomes increasingly important in the second region, where the fusion cross-section departs from the total reaction cross-section. A model describing this behavior is the one proposed by Glas and Mosel [1,2] that, with the same potential in (1.1) and the condition of $l > l_{CR}$, introduces a critical distance R_C as an additional condition for the fusion occurrence, limiting the number of partial waves leading to fusion. Figure 1.4 shows the

effective potential trend in region 2 and the critical distance R_C that has to be reached in order to lead the system to the fusion.

Another model, known as "Statistical Yrast Model" [17], suggests that the fusion is possible if the CN is formed above the "Statistical Yrast" line, a curve parallel to the usual Yrast line but few MeV shifted up (see fig. 1.5).

In the third region the compound nucleus (CN) formed in the fusion reaction becomes unstable against fission and owes to a sharp decrease of the fusion excitation-function.

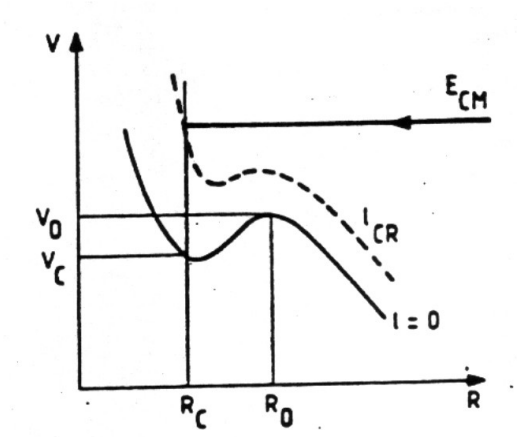

Fig 1.4 *In region 2 the model proposed by Glas and Mosel introduces a critical distance R_C. The fusion occurs only for the partial waves that lead the system to reach R_C.*

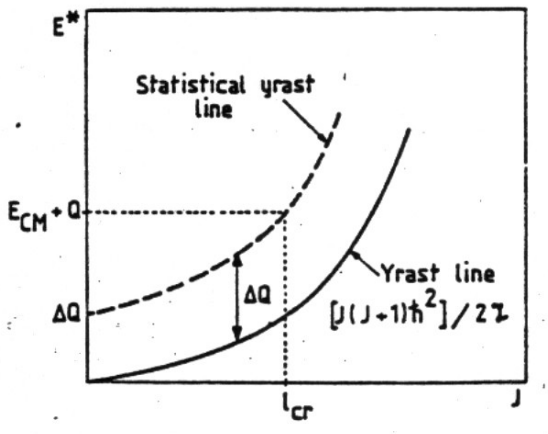

Fig. 1.5 *The statistical yrast line is few MeV shifted up with respect to the usual yrast line. As suggested by the model, the CN can be formed only above the statistical yrast line.*

1.2 The fusion process below the Coulomb barrier and channel coupling

Differently by the classical case discussed in the previous paragraph, in which the potential barrier is assumed to be crossed only if the incident energy is greater than the barrier itself, the quantum mechanics shows the existence of a non-null probability that a particle with a sub-barrier incident energy passes through the barrier. A simple approach (e.g. [79]) at the base of the single barrier penetration model (SBPM) consists in the resolution of the Schrödinger equation with the potential in (1.1) under the condition that the two colliding nuclei are spherical and with no internal structure. Since the symmetry of the system is spherical, the Schrödinger equation for the only radial part of the wavefunction $\chi_l(r)$ is

$$\frac{d^2\chi_l(r)}{dr^2} + \frac{2\mu\left[E_{CM} - V_l(r)\right]}{\hbar^2}\chi_l(r) = 0 \tag{1.7}$$

The Wentzel-Kramers-Brillouin (WKB) approximation allows to calculate the fusion cross section as the sum of the contribution of several transmission probabilities T_l, one for each partial wave involved in the description of the fusion process:

$$T_l(E) = \frac{1}{1 + e^{2K(E)}} \tag{1.8}$$

where

$$K(E) = \int_{r_1}^{r_2} \sqrt{\frac{2\mu}{\hbar^2}\left[V_l(r) - E\right]}\,dr \tag{1.8.1}$$

is integrated between r_1 and r_2, the values where $V_l(r_1) = V_l(r_2) = E$.
With the T_l probabilities, the fusion cross-section can be written as

$$\sigma_{fus}(E) = \frac{\pi}{k^2}\sum_l (2l+1)T_l(E) \tag{1.9}$$

The evaluation of T_l indexes with the potential (1.1) is sufficient to calculate the fusion cross-section in this energy region but, as discovered in the late 1970s [3] and early 1980s [4], at energies below the Coulomb barrier the experimental fusion cross-sections are

significantly increased with respect to the SBPM predictions. The reason for this behavior is the importance of the participant internal degrees of freedom in this range of energies [5]. The formation of CN at energies around and below the Coulomb barrier is indeed a complex phenomenon where each internal degree of freedom and therefore each reaction channel has a role. The arising importance of the participant internal degrees of freedom in the formation of the CN has the consequence that dynamical effects are observed on the fusion process. These effects arise from the coupling between several reaction channels, including inelastic excitations and direct reactions. The theoretical method to take into account the contribution of a number of reaction channels to the fusion cross-section is the coupled channel formalism (CC). This method consists in describing the wave function of the system as a sum of a number of components equal to the number of intrinsic quantum states involved [23,24]:

$$\left|\psi^{(+)}(\alpha_0 k_0)\right\rangle = \sum_\alpha \left\langle \alpha \middle| \psi_\alpha(\alpha_0 k_0)\right\rangle |\alpha\rangle \tag{1.10}$$

The notation $|\psi^{(+)}(\alpha_0 k_0)\rangle$ indicates that the collision is initiated in channel α_0, with wave vector k_0. The solution of the Schrödinger equation has components $|\psi_\alpha{}^{(+)}(\alpha_0 k_0)\rangle$ for each reaction channel α. For practical purposes, the infinite expansion is truncated so as to include only the most relevant channels. To account for the loss of flux through neglected channels, one may include a term $W_\alpha{}^D$ in the imaginary part of the channel potential $U_\alpha(r)$:

$$U_\alpha = V_\alpha + i\left(W_\alpha^D + W_\alpha^F\right) \tag{1.11}$$

where V_α is the real part of the potential and $W_\alpha{}^F$ takes into account for fusion absorption. Calculating the latter term one can evaluate the fusion cross section with [25-27]:

$$\sigma_F = \frac{k}{E}\sum_\alpha \left\langle \psi_\alpha \middle| W_\alpha^F \middle| \psi_\alpha \right\rangle \tag{1.12}$$

The effect of the coupling can also be introduced in the equation (1.9) since the transmission coefficients T_l depend on the matrix elements calculated with the CC calculations. As an example, Fig 1.6 shows the difference between the transmission

function calculated without the coupling effects and the same transmission function obtained considering a two-channels coupling [28,29].

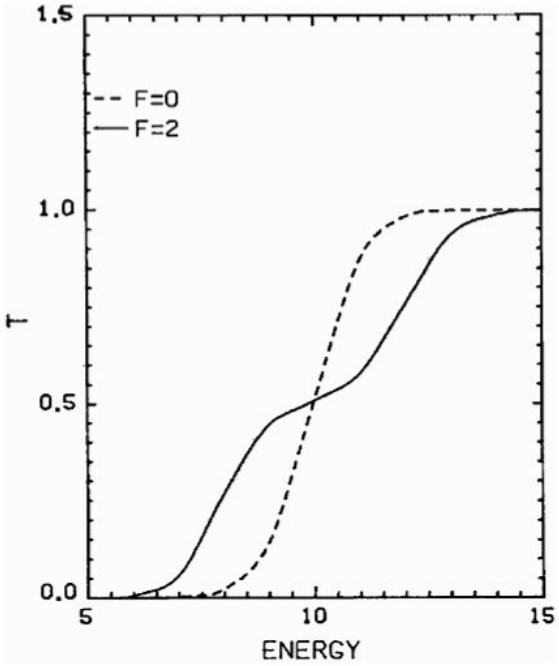

Fig. 1.6 *Calculated transmission functions for a two channels coupling case from refs [28,29]. The solid and dashed curves are calculated with and without coupling, respectively. The curves are expressed in arbitrary units.*

As observed almost thirty years ago, the fusion cross section at energies below the Coulomb barrier may be enhanced, in some cases by several orders of magnitude, by the effect of the couplings among several reaction channels [30-33].

Since in weakly bound nuclei the continuum is close to the ground state, it is necessary to represent the continuum in CC calculations. This is accomplished in the Continuum Discretized Coupled Channels (CDCC) calculations. In this case, the continuum that describes the break-up channel is discretized into bins [34,35].

1.3 General description of light weakly bound nuclei: halo and cluster structures

A weakly bound nucleus is a nuclear system with a ground-state energy very close to the particle emission threshold. This implies an increased probability for the break-up process, since a little excitation is sufficient to dissociate the projectile into two or more parts.

The low binding energy of the weakly bound system is also correlated to the structure of the nucleus, first of all its radius, which may be larger than expected [18] entailing a more

diffused matter distribution. There are weakly bound nuclei either stable (like ^{6}Li, ^{7}Li and ^{9}Be) or unstable (like ^{6}He, ^{11}Li and ^{11}Be). In such light nuclei, the experimental evidence for the cluster structure is well documented (see [19] and references therein). A cluster structure is characterized by the presence of two or more sub-systems in the nucleus. The simplest case of clusterization is that of the two α-particle system ^{8}Be. Systems such as ^{6}Li and ^{7}Li display ^{4}He+d and ^{4}He+t cluster structures, respectively.

The unstable weakly bound nuclei are created in modern accelerator laboratories and are close to the driplines [20], the limits of the nuclear landscape, where additional protons or neutrons can no longer be kept in the nucleus (they literally drip out). When approaching the driplines the separation energy of the last nucleon or pair of nucleons decreases gradually and the bound nuclear states come close to the continuum. The combination of the short-range nuclear force and the valence nucleons low separation energy results, in some cases, in a considerable tunneling of such nucleons into the classical forbidden region. The valence nucleon wavefunction shows a more or less pronounced tail corresponding to a diffused large region in the matter distribution as a function of the radius, the so-called nuclear halo state. [21,22] The nuclear halo is the extreme case of nuclear radius increase due to the low binding energy in weakly bound nuclei.

1.4 The fusion process in collisions involving weakly bound nuclei

As mentioned above, the two main properties of weakly bound nuclei are a low energy threshold for the break-up process and a diffuse matter distribution whose extreme case is represented by the halo nuclei. These properties are responsible of static and dynamical effects on the fusion cross-section around and below the Coulomb barrier. Static effects are due to the influence of the diffuse matter distribution on the projectile-target potential shape, reducing the Coulomb barrier and therefore leading to a possible fusion cross-section enhancement. The dynamical effects in collisions involving weakly bound nuclei appear because in the fusion, not only the coupling to bound states, but also the coupling to the continuum has to be taken into account. In fact the high probability for the break-up process makes it important in the coupled channel formalism. One of the most recent approaches, the CDCC formalism (Continuum Discretized Coupled Channels), based, as said above, on the continuum discretization in bins allows to take into account the break-up influence over the fusion process. As an example, Hagino et al. [63] calculated the fusion cross-section for the ^{11}Be+^{208}Pb system showing a sub-barrier

enhancement of complete fusion and its suppression above the barrier (fig. 1.7.1). Further accurate calculations [80] led to different results showing that the enhancement is present only very far below the Coulomb barrier.

So it is clear that there are theoretical and experimental difficulties in the study of reactions involving weakly bound nuclei.

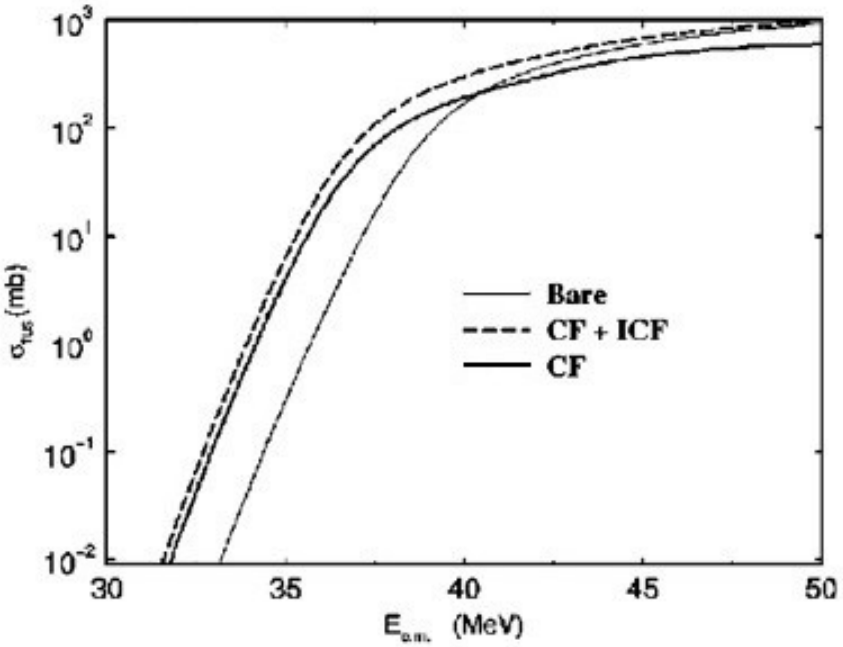

Fig. 1.7.1: *Fusion cross-sections calculations by Hagino et al. [63]. The calculation results show a sub-barrier enhancement with respect to the bare potential of the SBPM. For details see the text.*

In addition to these difficulties, since the projectile is weakly bound the scenario is further complicated by the presence of two different types of fusion: complete fusion (CF), when the whole masses of the projectile and the target are contained in the compound nucleus and incomplete fusion (ICF), when some nucleons move out of the interaction region before the formation of the CN. Another distinction has been made between the direct complete fusion (DCF) and the sequential complete fusion (SCF). The former consist of the formation of the CN by the direct collision of the projectile with the target; the latter is a process in which the fusion follows the projectile break-up but all fragments are captured by the target to form the CN. However, from an experimental point of view it is not possible to determine if the CN has been formed by SCF or DCF. Usually, in light nuclei, the ICF cannot be distinguished from other reactions such as transfer. Fig 1.7.2 shows a qualitative scheme of possible reaction channels in collisions involving weakly bound nuclei.

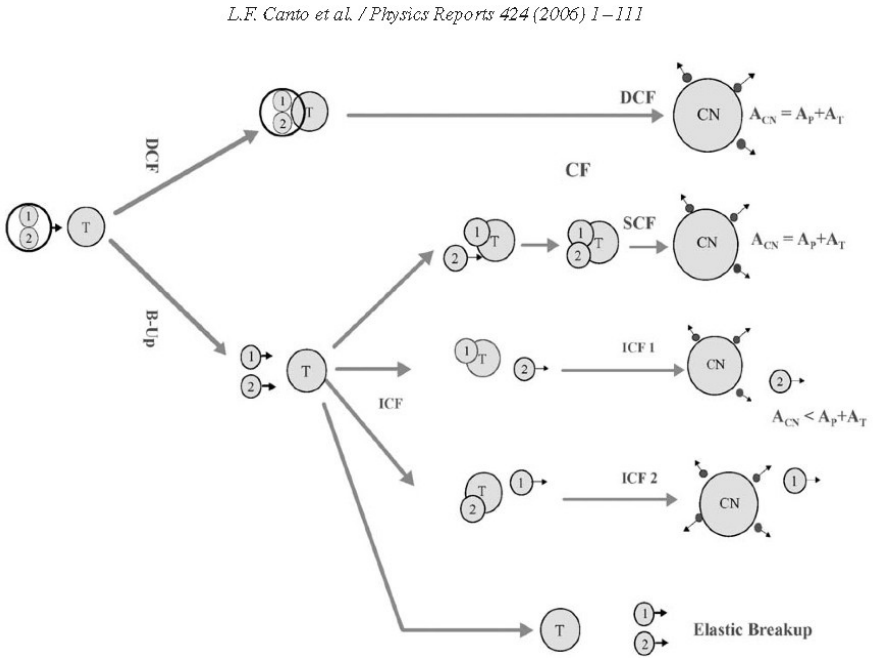

Fig 1.7.2 *Schematic representation, from ref [8], of the fusion and break-up processes that can take place in the collision of a weakly bound projectile. For simplicity is assumed that the break-up produces two fragments.*

1.5 Experimental techniques for measuring fusion cross-sections

The techniques to measure the fusion cross-section are classified into two categories: direct (ER or fission fragment detection) and indirect (γ-rays, α-particles, X-rays). In experiments using direct techniques, the fusion cross-section is measured detecting the charged ER or fission fragments produced in the decay of the CN. In experiments using indirect methods the fusion cross-section is measured detecting particles and radiation emitted by the CN decay or eventually originated in the successive decay of the ER.

Experiments involving unstable nuclei give data with low statistics because they are performed with low intensity beams of short-lived isotopes, typically of the order of $10^5 \div 10^7$ particles/s. That is, several orders of magnitude lower than the intensities of stable beams ($10^9 \div 10^{11}$ particles/s). Fusion experiments using either stable or radioactive beams may require the identification of each evaporation residue, through the determination of its atomic number Z and, if also possible, the mass number A. The most widely used techniques for this identification are based on ΔE–E and time-of-flight measurements.

The measurement of absolute cross-sections requires the determination of detection efficiency, solid angles, number of incident projectiles and number of target particles per cm^2. Alternatively, the absolute fusion cross-section can be obtained by comparison with

known cross-section of a process simultaneously measured in the same detection setup, typically the Rutherford scattering of the incoming projectiles.

1.5.1 Fusion cross-section measurements by direct methods

In order to obtain fusion cross-sections, it is necessary to measure the **ER angular distribution** and integrate it over angles. For this reason detection on a wide angular range can be needed. This condition can be achieved using large solid-angle detectors or using an appropriate experimental setup to cover the desired angular range. In order to collect the ERs, silicon detectors can be used. The principal disadvantage of the direct ER detection technique is the energy threshold of the detectors, the minimum energy that the ER must have to be detected. Moreover, in extreme cases of low bombarding energies, part of the produced ERs could not be able to emerge from the target and cannot be detected.

Since in a collision there are several simultaneous processes, it is necessary to separate the fusion products from the other non-fusion ejectiles by charge (and also mass number, if possible) identification for each detected ER. This discrimination can be done using ΔE-E telescopes as schematized in Fig. 1.8. The energy loss is proportional to the square of the ER atomic number Z and to its mass number A. From the two quantities E_R+ΔE and ΔE one can determine the total energy and the charge of the residue.

The ΔE resolution in this technique is often not enough to provide isotopic separation for a given atomic number Z. The mass identification can be therefore achieved by complementing the ΔE-E technique with **time-of-flight** measurements. This technique is based on the measure of the time interval that a particle takes to move between two detectors separated by a known distance as schematized in Fig. 1.9. Usually the start detector is a thin micro-channel plate, where the incident particle looses a very small amount of its energy and has a small angular dispersion when crossing it. Since

$$E = \frac{1}{2} m \cdot v^2 \tag{1.13.1}$$

The simultaneous measurement of ER energy and velocity allows extracting information on its mass A:

$$A \propto \frac{2E}{v^2} \tag{1.13.2}$$

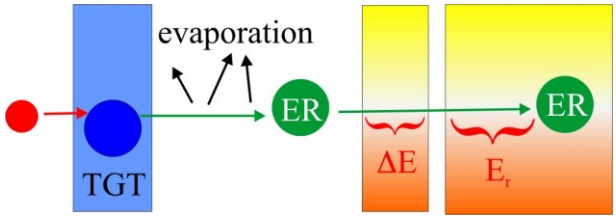

Fig. 1.8 *Schematic view of the direct ER detection technique. After the evaporation, the recoiling ER passes trough the two region of the ΔE-E telescope. The resultant two signals allow to identify the ER charge*

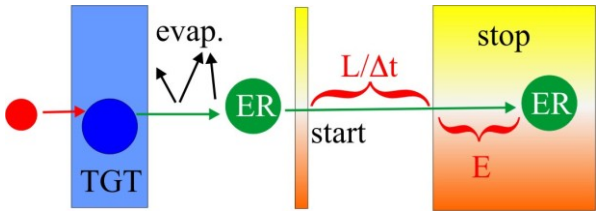

Fig. 1.9 *Schematic view of the time-of-flight technique.*

1.5.2 Fusion cross-section measurements by indirect methods

In the fusion of heavier systems the produced ER may decay emitting **α-particles** with half-lives ranging from few seconds to several months. In such cases, the evaporation channels can be identified by the on- and off-line detection of the isotropically emitted characteristic α-particles and the fusion cross section can be determined. The off-line technique is suitable for the detection of residues with half-lives long enough to allow the measurement of the activity. This technique is schematized in Fig. 1.10.

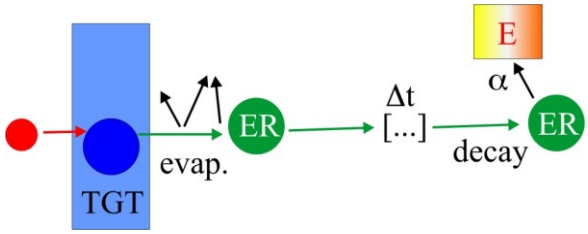

Fig. 1.10 *Schematic view of the off-line α-particle detection method. The characteristic energy of the emitted α-particle allows identifying the ER charge (and eventually its decay time) allows the isotope identification.*

In the fusion of lighter systems the ERs are not α-emitters. In some cases, depending on the colliding system, ERs are unstable nuclei and their production cross-sections can be extracted by the **off-line detection of the characteristic γ-rays** following their decay. In some cases the produced ERs decay by electron capture and their production cross-section

can be extracted by **off-line detection of the characteristic atomic X-rays** following the decay. This technique, schematized in fig 1.11, allows the ER identification by its atomic number Z and, following the activity curve for each ER charge Z, its mass number A, since different isotopes have different half-lives. In the experimental set-up for X-ray (or γ-ray) detection, a catcher foil is usually placed behind the target. This foil should be thick enough to stop the ER but it should let the scattered beam particles go through. After each irradiation, the target and catcher foil must be removed and placed in front of the X-ray (or γ-ray) detector.

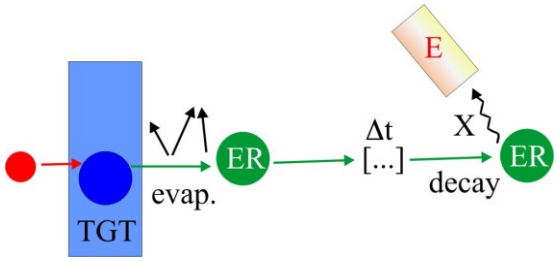

Fig. 1.11 *Schematic view of the off-line X-ray detection method. The characteristic X-ray emitted allows identifying the ER charge and its decay time allows the isotope identification.*

The **on-line γ-ray spectroscopy method** can be used in any mass region. This method, as schematized in Fig. 1.12, consists of the identification of fusion events through the detection of a characteristic γ-ray, emitted by the ER in the final phase of its de-excitation.

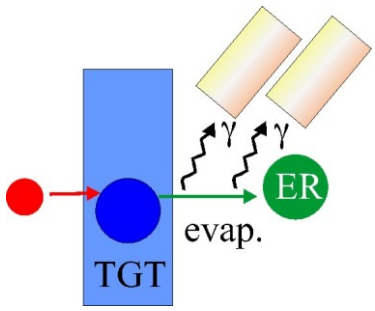

Fig. 1.12 *Schematic view of the γ-ray spectroscopy and/or off-line γ-ray detection method. The statistical analysis of the evaporation γ-rays allow the identification of the ERs. The characteristic γ-ray emitted allows identifying the ER charge and its decay time allows the isotope identification.*

The main objection to the application of the gamma-ray method to determine the fusion cross sections is that it uses a statistical model for the evaluation of the branching factors $\sigma_\gamma/\sigma_{ch}$ to obtain the channel and fusion cross-sections from the experimental gamma-ray

cross-sections. However, it is possible to justify the use of this procedure by determining the cross-sections for a specific channel using more than one γ-ray emitted from the same residual nucleus. A limitation of this method is that it misses those events that directly feed the ground state of the ER because in such cases no characteristic γ-ray is emitted [10].

1.6 Fusion involving weakly bound nuclei around the Coulomb barrier: some experimental results

In the last decade many experiments have been performed to measure fusion excitation functions in collisions involving weakly bound nuclei around the barrier. The fusion cross-section for a particular system results enhanced (or suppressed) when it is larger (or smaller) than some standard cross-section, to which it has been compared.

In this paragraph several results for collisions of weakly bound nuclei with heavy, medium and light targets will be summarized emphasizing, where possible, the used experimental techniques.

1.6.1 Collisions involving weakly bound nuclei and heavy mass targets

Several experiments have been performed concerning the study of complete and incomplete fusion cross sections in collisions induced by stable weakly bound nuclei around the fusion barrier [37,38,39,40,60]. Different authors agree on complete fusion cross-section suppression at energies above the Coulomb barrier by about 30% with respect to the SBP model or CC calculations without the break-up coupling (e.g. [37]). On the other hand it has been observed that the total fusion (i.e. CF+ICF, see paragraph 1.4) cross-sections appear, above the barrier, in reasonable agreement with the calculations. It has been therefore concluded that the observed suppression is due to the ICF following the projectile break-up. Conclusions of different authors regarding the possible presence of sub-barrier CF enhancement with respect to CC calculations not including continuum coupling (i.e. enhancement due to continuum coupling) do not show a clear systematic.

In the ^{6,7}Li+^{209}Bi and ^{9}Be+^{208}Pb systems, the ERs are α-active so the complete and incomplete fusion cross-sections are measured by the off-line α-particles detection [37,38]. The measured complete fusion cross-section shows a suppression at energies above the barrier with respect to the SBPM and to CC calculations, as shown in Fig. 1.13, 1.14 and 1.15. Below the barrier has been observed an enhancement with respect to the SBPM as expected but no effect with respect to the CC calculations without the coupling to the

continuum. As shown in Fig. 1.15, in the ^{9}Be case the observed suppression above the barrier vanishes when considering the total fusion (i.e. the sum of CF and ICF). The suppression has been also observed comparing collisions involving weakly bound nuclei with the collisions involving well bound nuclei forming the same compound nucleus as shown in Fig. 1.16.

Analogue results are reported in [39], for the ^{6}Li+^{208}Pb system studied by the same off-line α-particles detection technique of [37], and in [40], for the ^{6}Li+^{165}Ho system using the off-line γ-rays detection technique.

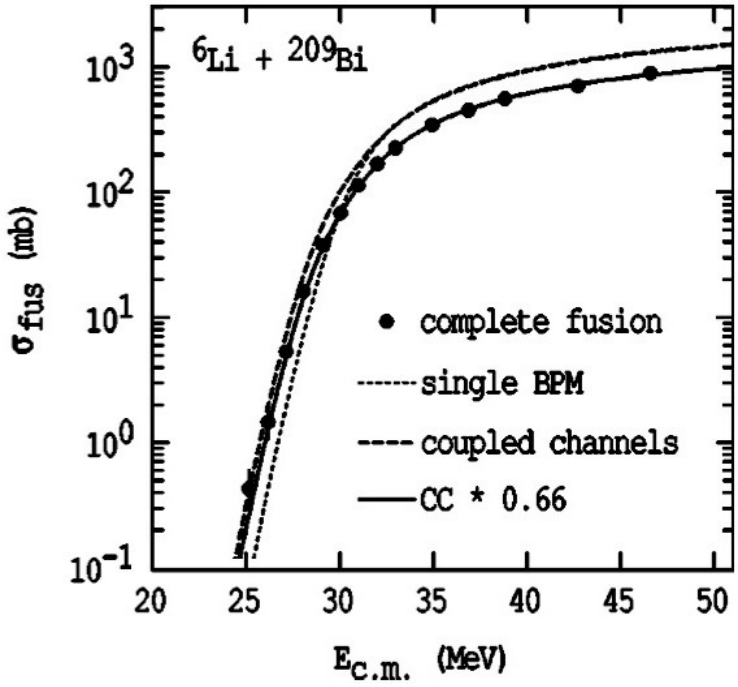

Fig. 1.13 *The measured complete-fusion cross-sections for the ^{6}Li+^{209}Bi system from ref [37]. The short dashed lines result from SBPM, while the long dashed lines show the results of CC calculations. The full line is the latter calculation scaled by the indicated factor.*

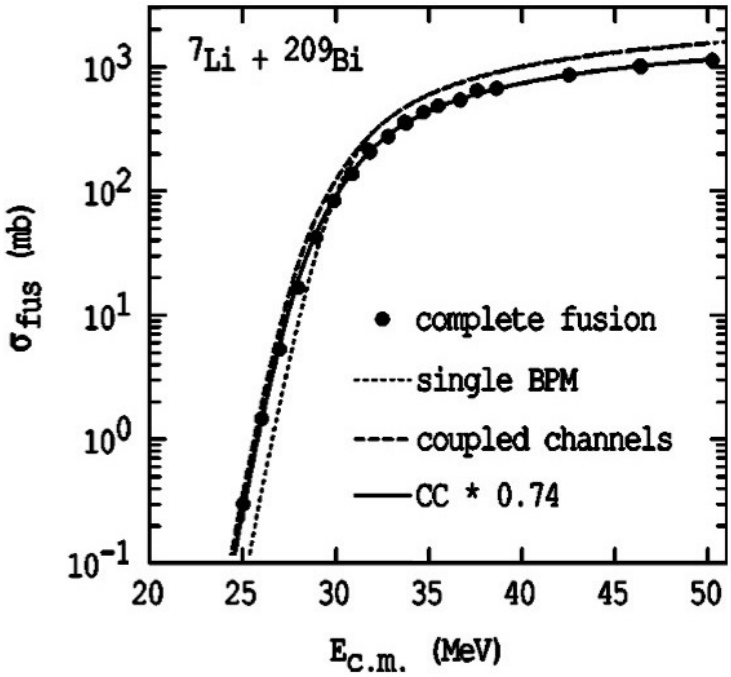

Fig. 1.14 *The measured complete-fusion cross-sections for the $^{7}Li+^{209}Bi$ system from ref [37]. The short dashed lines result from SBPM, while the long dashed lines show the results of CC calculations. The full line is the latter calculation scaled by the indicated factor.*

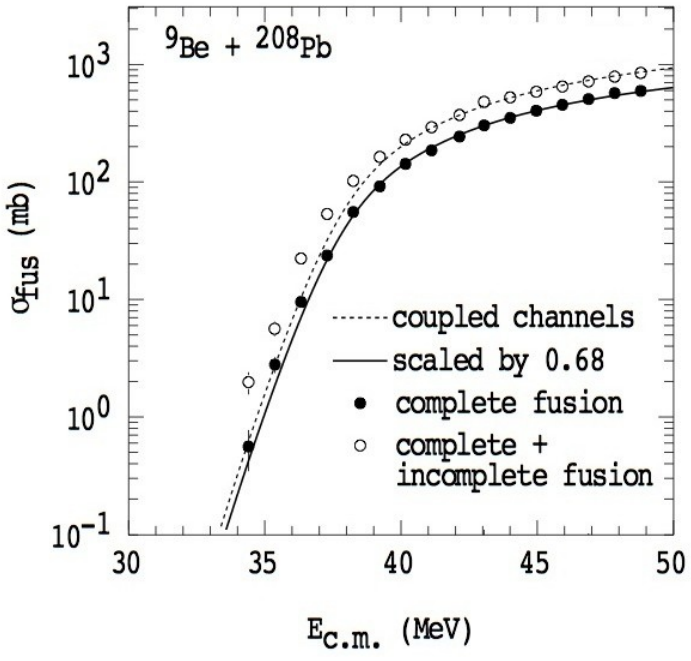

Fig. 1.15 *The excitation function for complete fusion (filled circles) for the reaction $^{9}Be+^{208}Pb$ from ref. [38]. The dashed line is the result of a CC calculation that ignores break-up effects. The full line is the same calculation scaled by a 0.68 factor. The empty circles give the sum of measured CF and ICF cross-sections.*

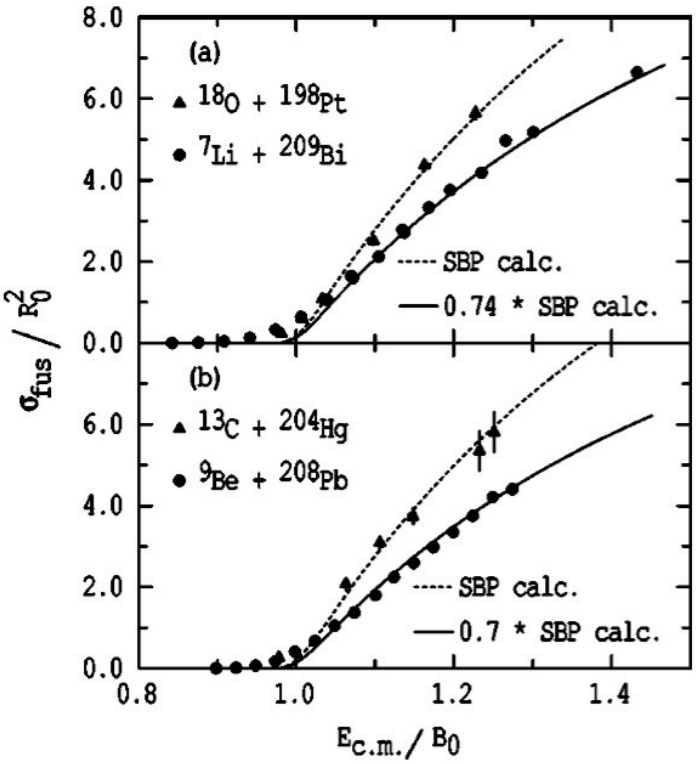

Fig. 1.16 *Experimental reduced CF excitation functions for (a) the $^{7}Li+^{209}Bi$ and $^{18}O+^{198}Pt$ reaction and (b) the $^{9}Be+^{208}Pb$ and $^{13}C+^{204}Hg$ reactions from ref. [60]. These show that CF cross-sections in collision involving weakly bound nuclei show suppression also with respect to reactions involving well bound ones forming the same compound nucleus. The dashed lines are SBPM calculations. The full lines are the calculations multiplied by the indicated factor.*

1.6.2 Collisions involving weakly bound nuclei and medium mass targets

In the collision of weakly bound nuclei on medium mass targets most of the experimental data concern total fusion cross-sections since CF and ICF can populate the same evaporation residues and their separation is difficult. However in those cases where the two contributions have been resolved it has been concluded that the ICF contribution is negligible. From the results of different authors it can be concluded that no effects are observed on the total fusion cross-section above the barrier whereas in the energy region below the barrier few data set exist and no systematic conclusions can be reached.

As an example, the total fusion cross-section for the $^{9}Be+^{64}Zn$ system has been measured with both the γ-ray and the time-of-flight methods obtaining concordant results [13]. As it can be seen in figure 1.17, where the total fusion cross-section is shown compared with the theoretical calculations and the total reaction cross-section, the authors observed no effects

at energies above the barrier but registered a slightly suppression around and just below the barrier. See the paragraph 1.9.1 for further examples.

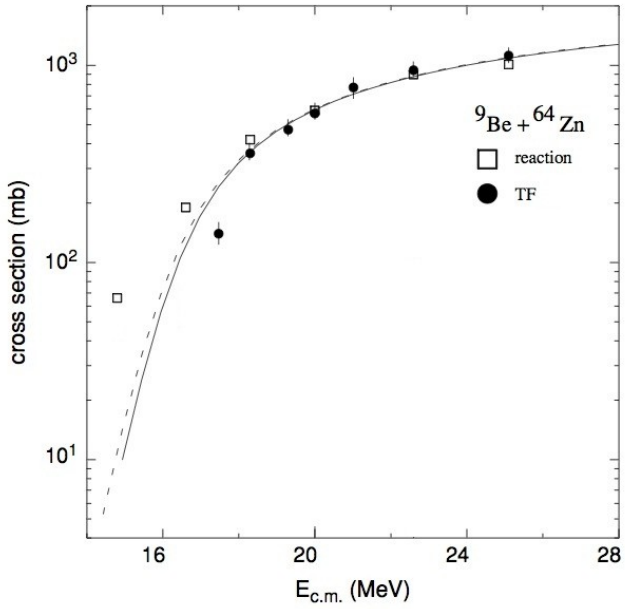

Fig. 1.17: *Total fusion and total reaction cross-sections for the $^9Be+^{64}Zn$ system as measured by [13]. The solid and dashed curves are results of CC calculations with and without coupling to the target excited states.*

1.6.3 Collisions involving weakly bound nuclei and light mass targets

Data from collisions of weakly bound nuclei on **light targets** are very limited at energies below the Coulomb barrier. In a systematic study [41] of ^{6,7}Li collisions on ^{9}Be and ^{12}C targets the fusion probability has been extracted as the ratio between the total fusion cross-section σ_F and the total reaction cross-section σ_R:

$$P = \frac{\sigma_F}{\sigma_R} \tag{1.14}$$

The experimental data have been acquired by the technique of direct ER detection, using a triple telescope consisting of a ionization chamber followed by two sequential solid state detector. The conclusion of such study was that for energies above the barrier there is a strong suppression of the total fusion cross-section with the fusion probability P (in Fig. 1.18) increasing as the break-up energy thresholds increase. However a more recent measure of the ^{7}Li+^{12}C collision [42], using the same technique of [41] but inverse

kinematics, shows a fusion cross-section several times larger than the previously measured one and is in agreement with the one measured by [43] with the γ-ray spectroscopy method (see fig. 1.19). The authors of [43] also suggested that the experimental method choice is crucial for a correct determination of the fusion cross-section. It has been concluded that there is no break-up suppression effect over the fusion cross-section of the $^{7}Li+^{12}C$ collision at energies above the Coulomb barrier (see Fig. 1.20). Following the results on this mass range it is now believed that the total fusion cross-section for collision of $^{6,7}Li$ and ^{9}Be on light mass targets shows a similar behavior as the one observed in the case of medium mass targets, that consist of no suppression effects above the barrier with lack of data at sub-barrier energies.

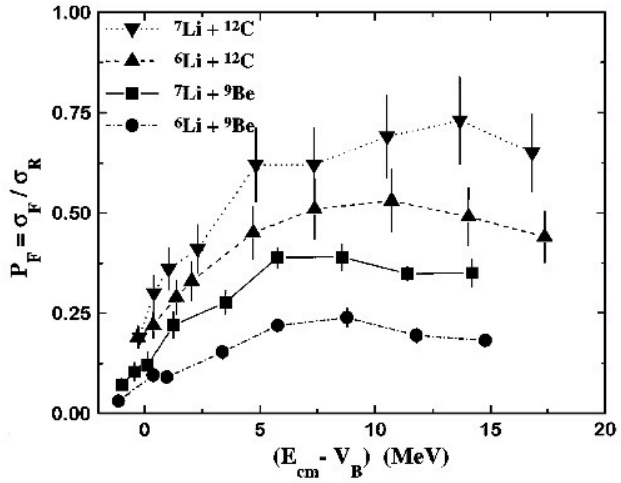

Fig. 1.18 *Energy dependence of the fusion probability $P_F=\sigma_F/\sigma_R$ for the $^{6,7}Li+^{12}C$ (triangles) and $^{6,7}Li+^{9}Be$ (respectively squares and circles) reactions from ref [41]. The lines were drawn to guide the eye. The error bars reflect the experimental uncertainty in σ_F, as well as the uncertainty in the σ_R determination from the optical model calculation. The decrease of P_F at higher energies (Ecm ≥ $4V_B$) due to the growing of important fast processes has not been investigated.*

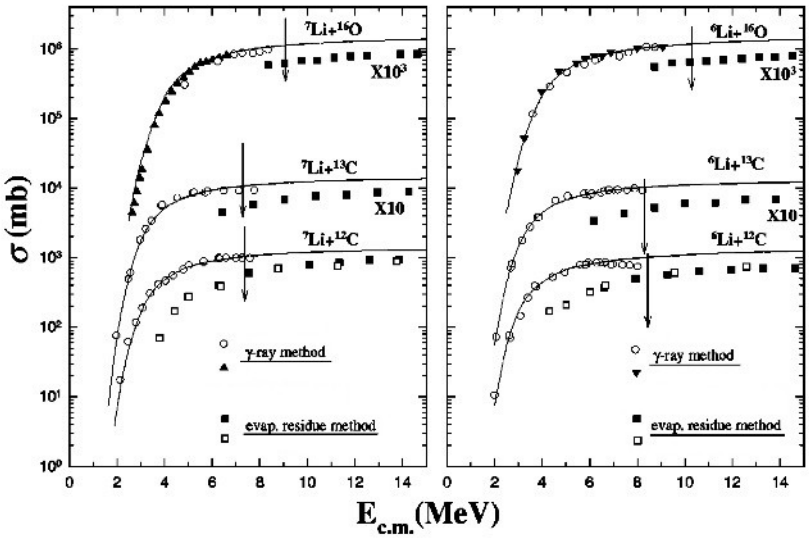

Fig. 1.19 *Total fusion cross sections for $^{6,7}Li+^{12,13}C$ and $^{6,7}Li+^{16}O$ reactions, measured by the γ-ray method in [43] (circles and triangles) and the evaporation residue detection method [41] (full and hollow squares). The solid lines represent the total reaction cross-sections calculated using optical model potential with parameters obtained from fitting the elastic scattering data. The arrows indicate the positions of two times the Coulomb barrier energy, up to which the fusion cross-sections are usually observed to be ≈ total reaction cross-sections. It can be noticed that data of [41] are systematically lower than ones of [43].*

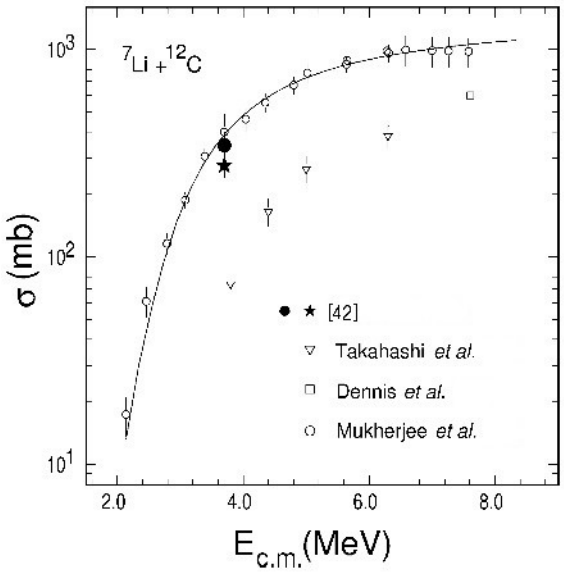

Fig. 1.20 *Fusion cross-sections for the $^{7}Li+^{12}C$ reaction from ref. [42]. The solid curve represents the optical model calculation obtained with parameters from Ref. [41]. The star represents the fusion cross-section measured, in [42] with inverse kinematics, from ERs having kinetic energies above 4 MeV. The filled circle includes a correction for the missing ERs with kinetic energies below 4 MeV. The hollow triangles are data from [41] measured by direct kinematics and does not agree with data measured by the gamma ray spectroscopy method (hollow circles and squares).*

1.6.4 Collisions involving halo nuclei

Measuring fusion cross-sections with low intensity radioactive beams is not an easy task. Most of the fusion cross-section data with halo beams existing so far have been measured using ^{6}He, since such beam is available with good currents at different facilities.

For some colliding systems such as ^{6}He on ^{209}Bi or ^{197}Au, the authors claim to observe an enhancement in the fusion cross-section below the barrier due to the halo structure of ^{6}He. For other systems like ^{6}He+^{238}U or the ^{6}He+^{64}Zn collision, which has been measured in [36] using the off-line X-ray detection technique, no enhancement effects have been observed. As an example, in figure 1.21 the fusion excitation function for the ^{6}He+^{64}Zn system is compared with the one extracted from the collision of the well bound ^{4}He on the same target. Within the explored energy range no effects due to the halo structure of ^{6}He have been observed but only a strong contribution of direct processes has been found, as shown in Fig. 1.22.

From the discussion so far, it follows that different authors did not reach similar conclusions about the presence of suppression/enhancement effects on the fusion cross-section due to the projectile halo structure. It has to be noticed however, that most of the existing data do not really explore the region below the barrier with a reasonable accuracy.

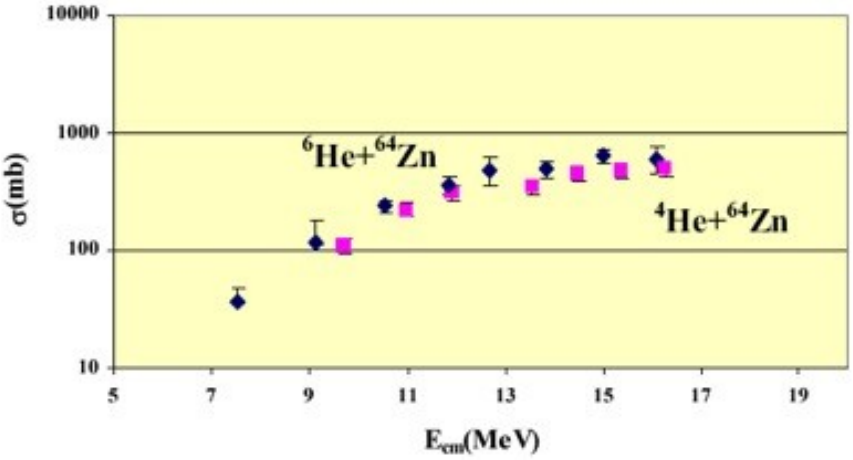

Fig. 1.21 *^{6}He+^{64}Zn and ^{4}He+^{64}Zn excitation functions in [36] obtained by summing up the contribution of all measured heavy reaction products except the ^{65}Zn contribution that has been replaced by the result from the statistical code CASCADE. Without the contribution of direct processes the two complete fusion cross-section appears to be equal.*

Moreover, conclusions of the published papers have been reached performing different type of analysis, and it is not always clearly discussed what role is played in the observed final result by the different static and dynamic effects. For this reason, a coherent analysis of different data sets would be desirable. In the following paragraph is presented an attempt to achieve this goal.

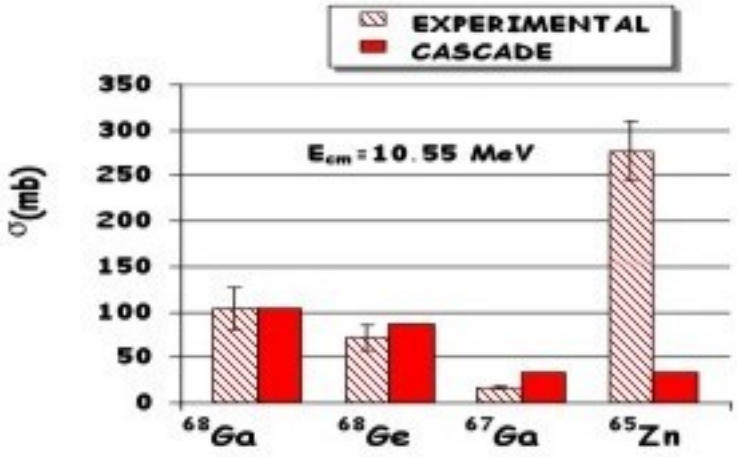

Fig. 1.22 *From [36], Comparison of the experimentally measured cross-sections of E.R. (dashed histogram) with the predictions of the statistical code CASCADE (full histogram) at E_{CM} = 10.55 MeV for the $^{6}He+^{64}Zn$ collision. The large ^{65}Zn yield suggests the presence of a large contribution from direct reactions also confirmed by particle coincidence [36].*

1.7 The "universal fusion function"

As already mentioned in the previous section, in order to conclude that the fusion cross-section is enhanced or reduced, it is necessary to compare the measured cross-section with a reference value. The fusion cross-sections can be compared to theoretical predictions like CC calculations or to the experimental data for well-bound systems forming the same compound nucleus. In the former case, the used theoretical calculations may differ in the number of effects considered (proper Coulomb barrier from realistic densities, coupling to bound states etc.) so the conclusions concerning the fusion cross-section may change drastically depending on the effects included in the CC calculation. If the calculations adopt a realistic optical potential and include the couplings to all relevant bound channels, the differences between theory and experiment can only result from break-up coupling. In the latter case, since different systems have different static properties (charge, mass and radius), the comparison result may differ depending on

the way used to perform the comparison itself. Usually the comparison is performed "reducing" the fusion excitation function in order to eliminate trivial effects due to the already mentioned static properties (different Coulomb barriers and radii of the considered systems) that vary from a system to another. For these reasons, in order to understand the effect of the coupling to the continuum, it is necessary perform a systematic study of fusion cross-sections for different systems involving weakly bound nuclei and to reduce the data according to some procedure and compare them to a standard universal benchmark.

A possible solution to this issue has been recently proposed [13,45]. To compare data for several systems in a single plot, it is necessary to eliminate the differences associated with trivial factors, like size and charge. This has been achieved by the introduction of the dimensionless energy variable x, substituting the energy, and a fusion function $F(x)$, substituting the fusion cross-section. $F(x)$ and x are defined as:

$$E' \to x = \frac{E - V_B}{\hbar\omega} \quad ; \quad \sigma'_F \to F(x) = \frac{2E}{\hbar\omega R_B^2}\sigma_F \tag{1.15}$$

Above, V_B, R_B, and $\hbar\omega$ are respectively the barrier height, the radius, and the curvature, obtained fitting, in the parabolic approximation, the projectile-target potential calculated using realistic densities. Similarly, also the fusion cross-section obtained by CC calculations σ_{CC} can be converted in a fusion function $F_{CC}(x)$:

$$\sigma'_{CC} \to F_{CC}(x) = \frac{2E}{\hbar\omega R_B^2}\sigma_{CC} \tag{1.15.1}$$

For systems where channel-coupling effects can be neglected and the fusion cross section is well approximated by Wong's formula [46], the substitution (1.15) in the Wong's formula leads to the Universal Fusion Function (UFF):

$$F_0(x) = \ln\left(1 + e^{2\pi \cdot x}\right) \tag{1.16}$$

In the same way the experimental fusion cross-section can be transformed into the fusion function $F_{exp}(x)$ using the substitutions in formula (1.15) and the comparison with the UFF can be made. Such a comparison of $F_{exp}(x)$ with the UFF indicates the global effect of

channel coupling on the fusion cross section. In this way, break-up couplings are entangled with couplings with other bound channels. To single out the effects of breakup coupling and eliminate deviations arising from the inaccuracy of Wong's formula at sub-barrier energies, it is necessary to renormalize the experimental fusion function as

$$F_{\exp}(x) \to \overline{F}_{\exp}(x) = F_{\exp}(x)\frac{F_0(x)}{F_{CC}(x)} \tag{1.17}$$

The ratio between $F_0(x)$ and $F_{CC}(x)$ is equivalent to the ratio between σ_0 (Wong's cross-section) and σ_{CC}.

The authors applied the UFF comparison to several collisions involving stable and unstable weakly bound nuclei on light (Fig. 1.24), medium (Fig. 1.25) and heavy (Fig. 1.23) targets. In the case of heavy targets, the complete fusion cross-section turns out to be suppressed at energies above the barrier. At energies below the Coulomb barrier the total fusion cross-section results enhanced with respect to the UFF. A similar comparison concerning the total fusion does not show any suppression above the barrier.

In the case of light and medium targets, apparently no effect has been observed at energies above the Coulomb barrier. Data below the Coulomb barrier are very limited and no conclusions can be still reached. Note that in collisions of weakly bound nuclei on light and medium mass targets most of the experimental cross-sections are total fusion cross-sections.

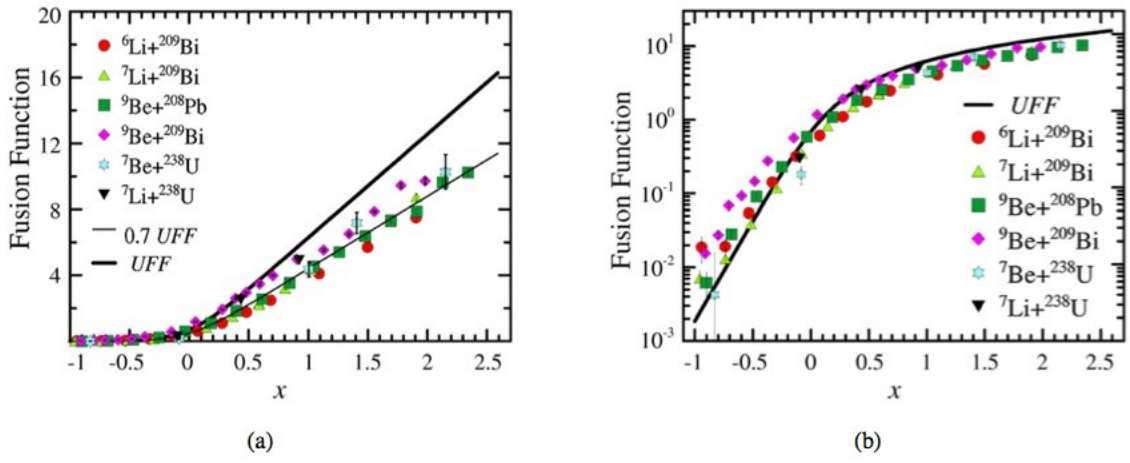

Fig. 1.23 *Comparisons of* $\overline{F}_{\exp}$ *in (1.16) based on CF data of [45] with the UFF (1.15) for collisions between weakly bound nuclei and heavy targets. The results are shown in (a) linear and (b) logarithmic scales.*

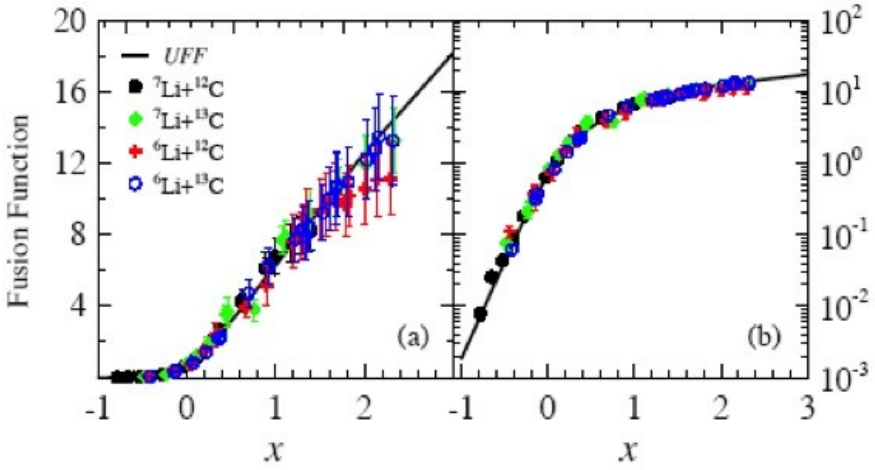

Fig. 1.24 *Experimental TF cross-section for the $^{6,7}Li+^{12,13}C$ systems show as an example of the UFF comparing method on collision involving light targets. The solid line represents the UFF.*

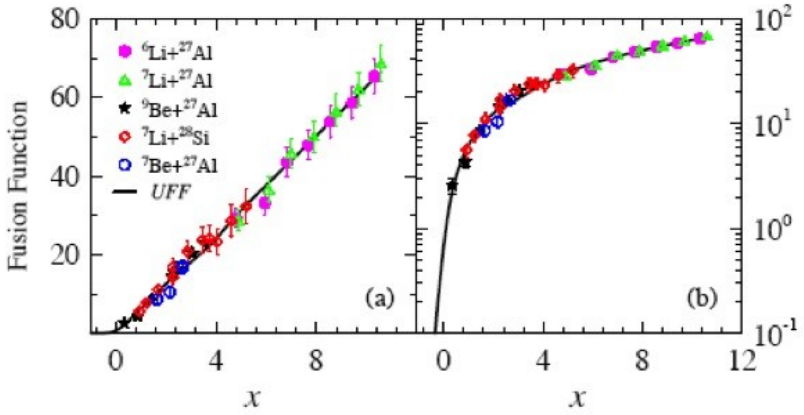

Fig. 1.25 *Experimental TF cross-section for collision involving medium targets. The solid line represents the UFF.*

1.8 Threshold anomaly and weakly bound nuclei

The Optical Model (OM) describes the interaction of the projectile with the target by a complex optical potential (OMP) U in which the imaginary part W is relative to the absorption by non-elastic processes:

$$U(r)=V(r)+iW(r) \tag{1.18}$$

where r is the radial distance between the two participants. The function that describes the real part $V(r)$ can be chosen between several kinds of potential. The most common ones are

the empirical Woods-Saxon (WS) [47] and the Double Folding (DF) [48]. The former is in the form

$$V(r)=\frac{V_0}{1+e^{\frac{r-R}{a}}} \tag{1.19}$$

where V_0 is the potential depth, a is the diffusivity or "surface thickness" and R the nuclear radius. The latter is the convolution of the participants matter distributions $\rho_1(r)$ and $\rho_2(r)$ with the nucleon-nucleon potential $V_{NN}(r_{12}=r-r_1+r_2)$:

$$V(r)=V_0\iint \rho_1(r_1)\cdot\rho_2(r_2)\cdot V_{NN}(r_{12})dr_1dr_2 \tag{1.20}$$

where V_0 is the potential strength or "normalization factor". For the imaginary part $W(r)$ it is possible to use also a WS potential or the same DF as the real part but with a different normalization factor. In some cases $U(r)$ is a combination of Woods-Saxon and Double Folding potentials. Fitting the angular distribution of the elastic scattering using the optical model potential, it is possible to evaluate the parameters of the chosen potential and the normalization factor for both the real and the imaginary parts.

At energies well above the Coulomb Barrier, the optical model potential assumes a constant value or a smooth, slow variation with the center-of-mass energy E. Decreasing the center-of-mass energy to values around and below the barrier, a different behavior has been observed. In the region around the Coulomb barrier, the strength of the imaginary potential $W(r)$ decreases rapidly as the energy is reducing. This behavior has been explained with the closure of the non-elastic processes that cannot take place because the energy is not sufficient, leaving the colliding ions apart. This reduction of the imaginary part strength has been observed to be accompanied, over the same energy range, by a rapid increase in the strength of the real potential as the center-of-mass energy is reducing [49,50]. Later observations [51,52] evidenced that the magnitude of the real potential begins to decrease again as the energy falls below the top of the nominal Coulomb barrier, so that a curve of its strength versus energy shows a bell-shaped maximum in the vicinity of the Coulomb barrier. The above-described phenomenon has been called "Threshold Anomaly" (TA) and is shown in fig. 1.26, as the trend of the real and the imaginary part of the optical model potential.

The effect observed in the real part is due to the presence of coupling to other channels and it can be taken in account introducing a *dynamic polarization potential ΔV(E)* [53] so (1.17) becomes:

$$U(r)=V(r)+\Delta V(E)+iW(r) \tag{1.21}$$

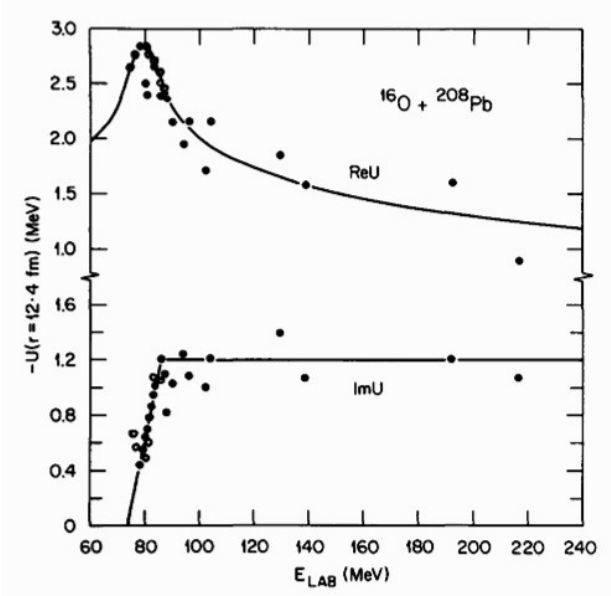

Fig. 1.26 *Usual behavior of the threshold anomaly as a function of the incident energy from Ref [53] about the $^{16}O+^{208}Pb$ system. See the text.*

In the "usual" TA, observed for collisions between well-bound nuclei, the dynamic polarization potential is attractive and the optical model potential (OMP) trend with the energy is the same independently of the real and the imaginary parts of potentials for the elastic data fit.

The real and the imaginary part are linked together by the dispersion relation [54] so a rapid variation in the real potential implies a rapid variation in the imaginary potential and vice versa:

$$V(r,E)=\frac{\mathbf{P}}{\pi}\int\frac{W(r,E')}{E'-E}dE' \quad \text{and} \quad W(r,E)=-\frac{\mathbf{P}}{\pi}\int\frac{V(r,E')}{E'-E}dE' \tag{1.22}$$

where **P** denotes principal value.

Since in collision involving weakly bound nuclei the coupling with the break-up channel becomes important, the polarization potential may result radically different as suggested in

[55]. In particular, the coupling to break-up channel produces a repulsive polarization potential and the usual TA trend may disappear. For this reason several works have been devoted the study of elastic scattering in the vicinity of the barrier for weakly bound systems [e.g. 56-58] and in most of them no usual threshold anomaly has been observed (e.g. Fig. 1.27). In some cases the extracted energy dependence of the real and the imaginary parts around the barrier is rather constant. In other cases, one can even find an increase of the imaginary part and, correspondingly, a small decrease in the real part.

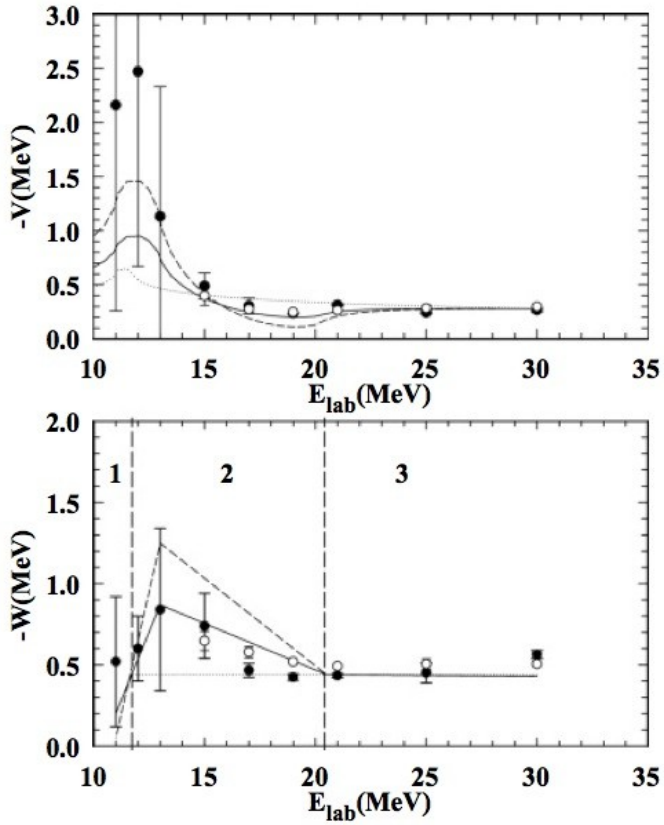

Fig. 1.27 *Normalization factors, from ref [71], of the real and imaginary potential for $^{6,7}Li+^{90}Zr$ as a function of the lithium bombarding energy. The usual TA is clearly not present anymore.*

As already mentioned, the usual experimental approach to study the effects of the coupling with the break-up and other reaction channels on TA for weakly bound nuclei consists of the elastic scattering angular distribution measure. In this technique one uses sets of movable detectors allowing the identification of the scattered particles (i.e. silicon barrier or position sensitive ΔE–E telescope or a spectrometer) in order to cover a wide angular range. In order to precisely determine the scattering angle, collimators or masks are frequently placed in front of the detectors. The elastic scattering angular distributions measured at different energies are then fitted using the chosen OMP in order to obtain the

potential parameters and the normalization factors that show, in their trend with the energy, the TA. In some cases more than one kind of potential is used in order to check the procedure consistency confirming that the OMP trend with the energy is independent by the chosen potential.

The OM analysis of the elastic scattering also allows extracting the total reaction cross-section that is useful to study the importance of non-fusion channels. In fact, since the total fusion cross-section must be below the total reaction cross-section, the difference between the two cross-sections is due to the non-fusion channels like the EBU. The measure of the elastic scattering angular distributions at low energies is a difficult task because, in this case, the Coulomb scattering is dominant. Therefore, to observe small variations with respect to the pure Coulomb scattering it is necessary to measure with accuracy of the order of 1% extending data collection to very backward angles.

As it will be discussed in the paragraph 1.9.2 the coupling effects on the threshold anomaly in collisions involving weakly bound nuclei are still not completely clarified. No systematic behavior has been observed in the studies performed so far and more precise data around the barrier are surely needed.

1.9 Motivations and goals of this work within the discussed topics

As already seen in the discussion so far, the study of reaction mechanisms in collisions involving weakly bound nuclei presents many new interesting aspects that are not still completely clarified. The stable ^{6}Li and ^{7}Li weakly bound nuclei are good candidates to investigate on such effects. ^{6}Li presents an α+d cluster structure with no bound excited states [11] and has a separation energy of S_α = 1.48 MeV [37]; ^{7}Li has an α+t cluster structure with a separation energy of S_α = 2.54 MeV [60] and a bound excited state at E = 478 KeV. Studying the collisions induced by both isotopes on the same target it is possible to search for possible differences due to their different structure. In the following chapters the results from a set of experiments, concerning the fusion cross-section and the elastic scattering angular distribution measurement for the ^{6,7}Li+^{64}Zn systems, will be discussed.

1.9.1 Fusion excitation functions for the ^{6,7}Li+^{64}Zn systems

The ^{6,7}Li+^{64}Zn fusion excitation functions have been already studied at energies around and above the Coulomb barrier [62]. The experimental technique used by these authors is

the direct ER detection by the time-of-flight technique. As it can be seen in figures 1.28 and 1.29, the measured total fusion cross-section results rather small with respect to the total reaction-cross section. Consequently the elastic break-up cross-section would be rather large contrary to the behavior of other systems like, for instance, the collision involving the weakly bound ^{9}Be on the same target (e.g. figure 1.20).

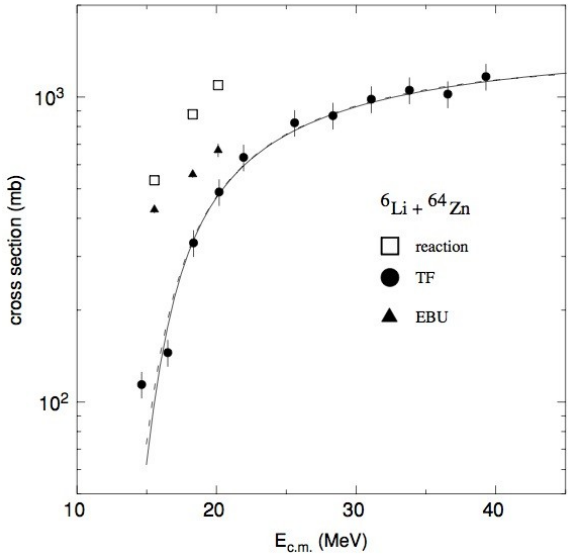

Fig. 1.28: *Total fusion and total reaction cross-sections for the ^{6}Li+^{64}Zn system as measured by [13]. The anomalous large difference between the two cross-sections would lead to an unexpectedly large break-up cross-section (EBU).*

The authors concluded that at energies above the barrier, ^{6,7}Li break-up at relatively large distances from the target, and their fragments move in different directions, leading to a significant elastic (non capturing) break-up cross-section.

As observed by the same authors of [13] in [14], the ^{6,7}Li+^{64}Zn fusion data are not following the systematic behavior of other analogue systems and, in particular for the ^{6}Li+^{64}Zn system, data are showing suppressed values with respect to the UFF as shown in fig. 1.30. The authors therefore suggested in [14] that the existing data might be affected by a systematic error, so further measurements are needed.

For these reasons the first goal of this work is to measure again the fusion excitation function for the ^{6,7}Li+^{64}Zn systems using a different experimental technique in order to avoid the energy threshold problems linked to the direct ER detection method. In addition, avoiding this energy threshold it is possible to extend data at energies far below the Coulomb barrier highlighting possible effects due to the different structure of ^{6}Li and ^{7}Li. Such kinds of effects have been observed in the study of fusion excitation functions for the

^{6,7}Li+^{59}Co systems [12] at energies around and above the Coulomb barrier. Here the authors found that the ^{6}Li fusion cross-section increases with respect to the ^{7}Li one as the energy is reducing (see Fig. 1.31).

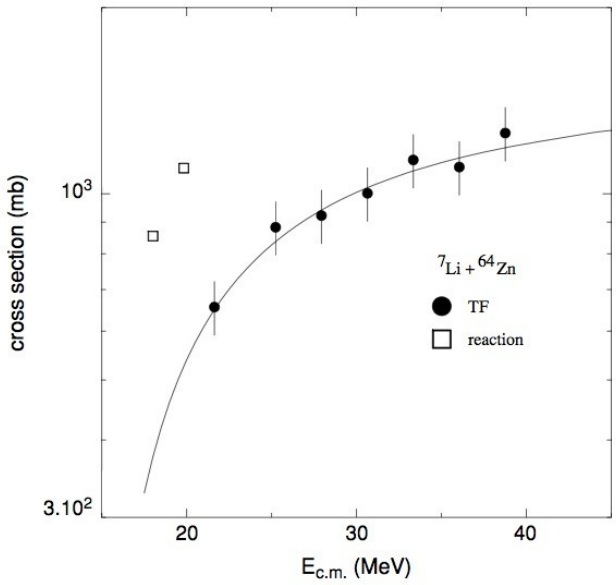

Fig. 1.29: *Total fusion and total reaction cross-sections for the ^{7}Li+^{64}Zn system as measured by [13].*

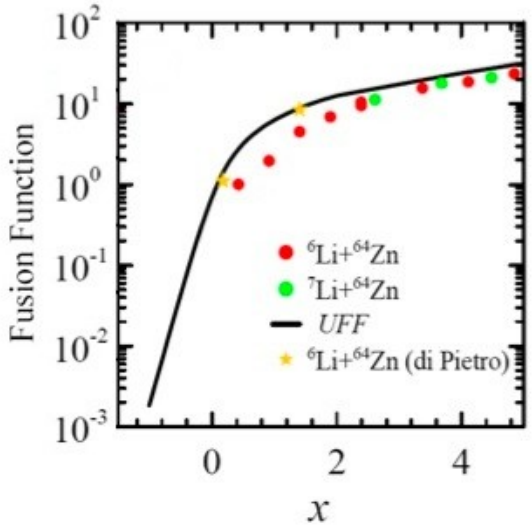

Fig. 1.30 *The experimental data for the ^{6,7}Li+^{64}Zn systems seems to not agree with the systematic behavior of similar systems. Further investigations are needed for this system. The solid line is the UFF.*

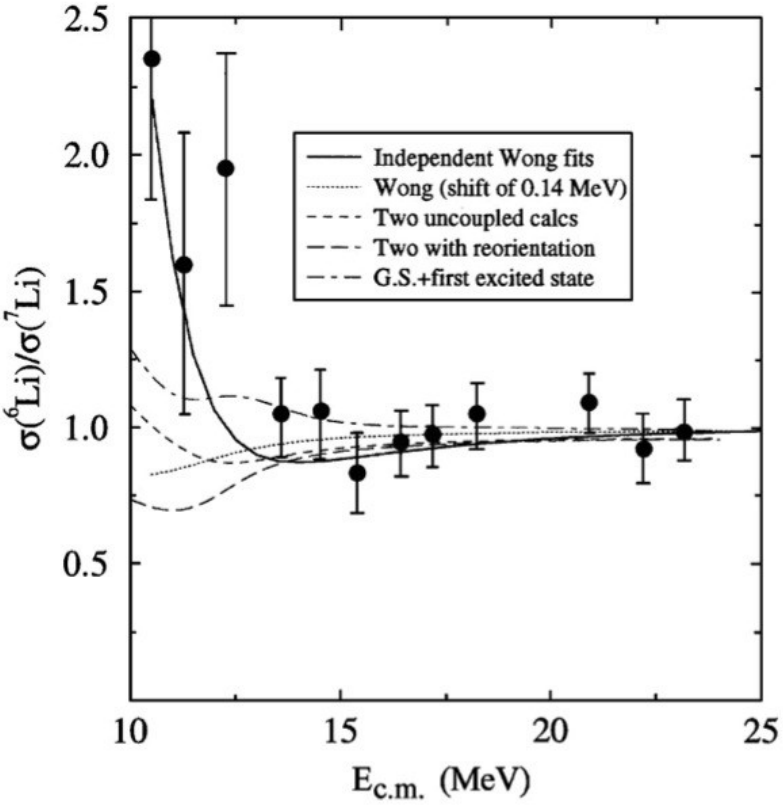

Fig. 1.31 *Energy dependence of the ratio of the total fusion cross-sections for $^{6}Li+^{59}Co$ and $^{7}Li+^{59}Co$ reactions from ref [12]. Error bars reflect the large systematic errors. The solid and dashed curves correspond to SBPM fits of the ratios. The dotted curves correspond to two uncoupled CC calculations with and without reorientation effects, whereas the dot-dashed curve is the result of CC calculations including the coupling to the first excited state.*

In a further theoretical study [44] based on the CDCC approach, the authors concluded that this behavior could be explained only considering the coupling with the break-up channel and that it is due to the lower break-up threshold of ^{6}Li when compared to ^{7}Li. Another goal of this work is to check for a similar behavior also in collisions involving the ^{64}Zn target.

1.9.2 Threshold anomaly for the $^{6,7}Li+^{64}Zn$ systems

As already mentioned in paragraph 1.7, it is well known that the optical potential extracted from the analysis of the elastic scattering of heavy ions, involving tightly bound nuclei, shows a rapid energy variation at energy near the Coulomb barrier, the so-called threshold anomaly (TA) [53,54]. Recently, much work has been devoted to the study of the TA in elastic scattering of the ^{6}Li and ^{7}Li weakly bound nuclei. For these projectiles the coupling

to the break-up produces a repulsive polarization potential [56] and the usual TA may, in this case, disappear. The effects of the break-up channel on the elastic scattering of ^{6}Li and ^{7}Li have been studied for different target nuclei [7,57,58,59,67,68,69]. Some authors [e.g. 9,53,54,59] observed an opposite behavior (i.e. the rise of the imaginary part and the decrease of the real one when the energy decreases approaching the barrier) with respect to the "usual" TA and this has been called "Break-up Threshold Anomaly" (see e.g. fig. 1.27). However, conclusions regarding the presence or absence of the usual threshold anomaly in collisions involving weakly bound nuclei are still contradictory.

Keeley et al. [57] have investigated the elastic scattering of ^{6}Li and ^{7}Li on ^{208}Pb at energies around the Coulomb barrier. Fitting data with Woods-Saxon potentials it has been found that the energy dependence of the optical potential is consistent with the existence of the usual TA for the ^{7}Li projectile and its absence for the ^{6}Li projectile, as shown in fig. 1.32.

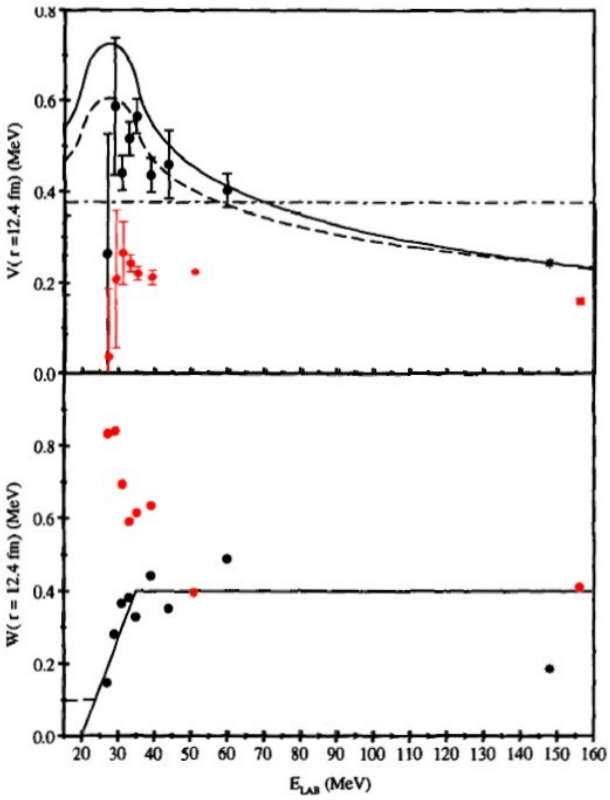

Fig. 1.32: *Optical model potential trend with the incident energy obtained fitting with a Woods-Saxon potential the elastic scattering angular distribution for the ^{7}Li+^{208}Pb system (black) and the ^{6}Li+^{208}Pb one (red) from ref [57].*

The same result has been confirmed by [58] using the Double Folding potential. The data for the ^{6}Li+^{208}Pb system where also re-analyzed by Hussein et al. [59] and the results for

the energy dependence of the optical potential have been interpreted as an evidence of the break-up threshold anomaly. Maciel et al. [7] measured the elastic scattering of ^{6,7}Li+^{138}Ba at near barrier energies. The results of the optical model analysis are similar to those for the ^{208}Pb target [59]. The presence of the usual TA for the ^{7}Li elastic scattering has been interpreted as the effect of the strong couplings with the first excited state of the ^{7}Li (0.48 MeV) inelastic channel, and other direct and inelastic channels, leading to an attractive polarization potential. The ^{6}Li nucleus has a break-up threshold energy of 1.48 MeV, hence the break-up channel is expected to be the dominant direct reaction channel. Gomes et al. [8] re-analyzed the ^{6,7}Li+^{138}Ba data. The results suggest the presence of the break-up TA for both projectiles.

Elastic scattering of ^{6,7}Li nuclei on light targets ^{28}Si and ^{27}Al has been measured by Pakou et al. [58,67] and Figueira et al. [9,68], respectively. In the case of the ^{28}Si target, no usual TA has been observed. As an example the trend of the potentials for ^{6}Li+^{28}Si case is shown in fig. 1.33. Again, no usual TA has been observed for the ^{6,7}Li+^{27}Al systems. In particular the ^{6}Li+^{27}Al scattering suggests the presence of the break-up TA as shown in fig 1.34.

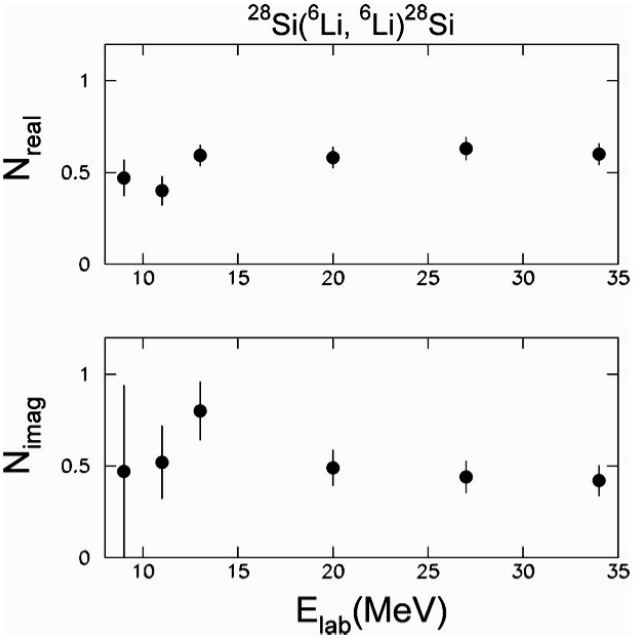

Fig. 1.33: *The energy trend of the real and the imaginary part of the OMP as measured by Pakou et al. from ref [67] for the system ^{6}Li+^{28}Si. No usual TA is observed.*

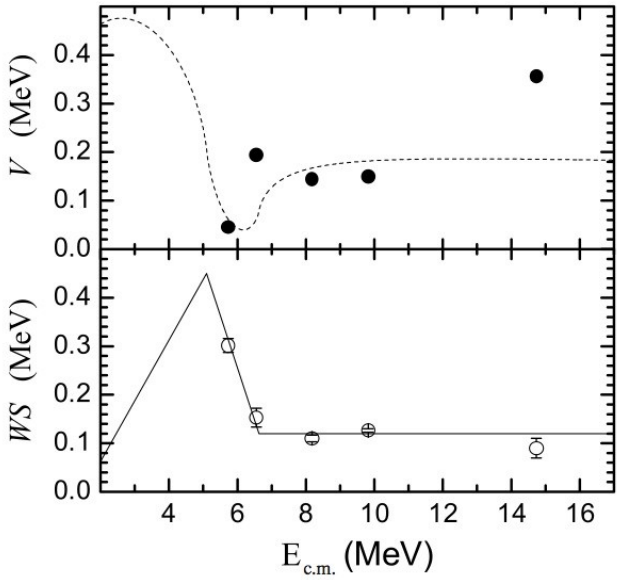

Fig. 1.34: *The energy trend of the real and the imaginary part of the OMP as measured by Figueira et al. from ref [9] for the ^{6}Li+^{27}Al system. The authors suggest the presence of the break-up TA.*

The study of the threshold anomaly in the elastic scattering of ^{6,7}Li on medium mass targets ^{59}Co[59,60,69], ^{58,64}Ni[70] and ^{90}Zr[71] has been recently performed. In the ^{6}Li+^{90}Zr system the break-up threshold anomaly has been found as shown in fig. 1.27. Data for other systems like the ^{6,7}Li+^{59}Co ones (shown in fig 1.35, 1.36) are not very clear since they do not cover properly the region around the barrier.

In summary, elastic scattering for the systems involving the weakly bound nuclei ^{6,7}Li have been studied for different mass targets. However, the available experimental data does not allow drawing general conclusions regarding the behavior of the optical potential around the Coulomb barrier. The results for many systems are not conclusive because there are not enough data available at near-barrier and/or sub-barrier energies and the uncertainty over the data are pretty large. Thus, it is important to perform measurements with small energy steps at energies in the vicinity of the Coulomb barrier. Moreover, at energies below the barrier the Coulomb potential dominates the elastic scattering. Therefore, high precision elastic scattering data, taken with careful minimization of possible systematic errors, are required in order to extract a reliable energy trend of the nuclear potential. For the reasons above discussed it has been decided to measure with high accuracy the elastic scattering angular distributions for the ^{6}Li+^{64}Zn and the ^{7}Li+^{64}Zn collisions and compare the data for the two systems.

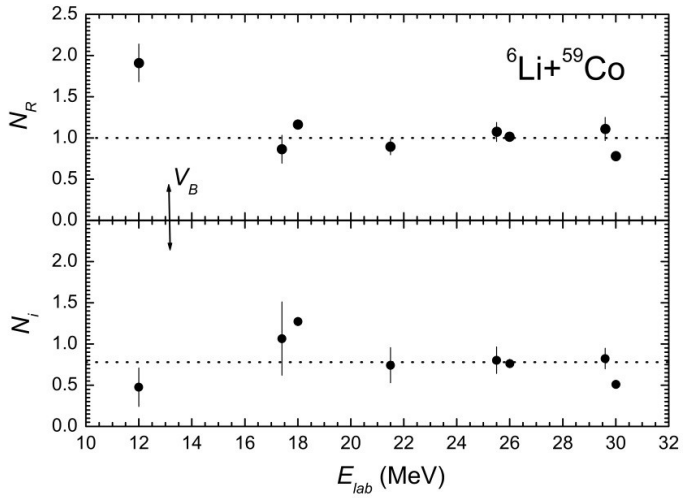

Fig. 1.35: *The energy trend of the real and the imaginary part of the OMP as measured by Souza et al. from ref [69] for the ^{6}Li+^{59}Co system. These authors suggested the presence of the usual TA in this system.*

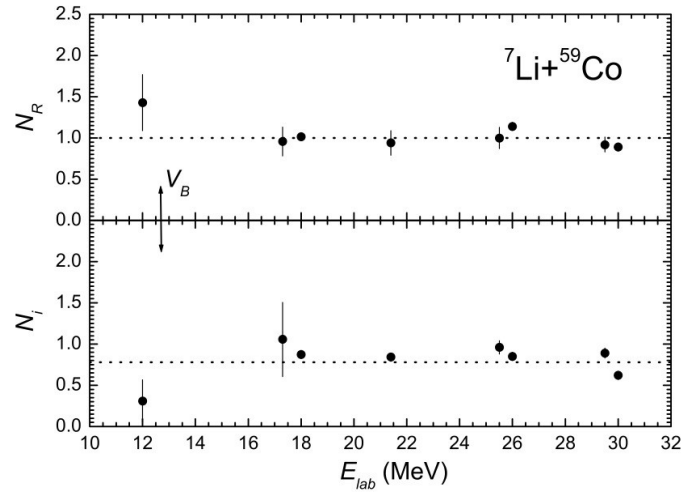

Fig. 1.36: *The energy trend of the real and the imaginary part of the OMP as measured by Souza et al. from ref [69] for the ^{7}Li+^{59}Co system. These authors suggested the presence of the usual TA in this system.*